Near-Surface Material and Topography Generate Anomalous High-Frequency Ground-Motion Amplification in Chugiak, Alaska

Te-Yang Yeh[*1,2], Kim B. Olsen[1], Jamison H. Steidl[3], and Peter J. Haeussler[4]

ABSTRACT

An ~3 km long nodal array oriented approximately east–west was deployed in Chugiak, Alaska, by the U.S. Geological Survey during 2021. The array intersects with the permanent NetQuakes station NP.ARTY, where peak ground acceleration (PGA) value of 1.98*g* was recorded during the 2018 M_w 7.1 Anchorage, Alaska, earthquake, in sharp contrast to the PGA of ~0.3*g* at a site just 4 km to the west. Seismic data for M_L 1.8–4.3 aftershocks from the M_w 7.1 event recorded by the nodal array confirm the anomalously large ground motions obtained at NP.ARTY as well as similar amplifications at nodes within ~1 km to the east. Here, we performed 0–10 Hz 3D finite-difference simulations, including high-resolution surface topography, to explore the cause of the unexpectedly large amplification. As expected, the simulations computed with a regional 3D tomography velocity model severely underpredict the 0–10 Hz acceleration records at almost all sites. Adding a near-surface low-velocity taper to 300 m depth amplifies the accelerations by up to a factor of 5 and enables a reasonable match between the nodal data and simulations at sites to the west of NP.ARTY. However, this model still underpredicts the spectral energy in the area covered by glacial sediments by up to an order of magnitude. The addition of a till layer using a depth-dependent shear-wave velocity (V_S) profile along with a homogeneous, 8 m thick low-velocity layer with $V_S = 250$ m/s representing the kame terraces improves the fit to data to within a factor of 2 at nodes located on top of the glacial sediments. Our study shows that the anomalously large high-frequency amplification recorded at and near NP.ARTY can be explained by a combination of topographic effects and near-surface low-velocity material with amplification effects on the high-frequency ground motion by up to about 40% and an order of magnitude, respectively.

KEY POINTS

- We observed and simulated unexpectedly large seismic amplification recorded in Chigiak, Alaska.
- Strong amplification is caused by combined effects of local topography and shallow low-velocity material.
- Unexpectedly large amplification can occur outside sedimentary basins due to local geologic conditions.

Supplemental Material

INTRODUCTION

The 2018 M_w 7.1 Anchorage, Alaska, earthquake (see Fig. 1 for location) strongly affected the greater Anchorage area, causing ground failure, widespread power outages, structural and nonstructural damage to buildings, and damage to roadways and railways (Jibson *et al.*, 2019; Ruppert and Witter, 2019). Relatively large peak ground motions (>0.25*g*) were observed over an ~8000 km^2 area with substantial spatial variation due to local near-surface soil conditions (West *et al.*, 2019). Smith and Tape (2019) calculated amplification factors up to about 5 for earthquakes and ambient noise at frequencies less than 4 Hz, increasing at stations above the deeper parts of the Cook Inlet basin. Moschetti *et al.* (2019) analyzed seismic data from 44 intermediate-depth earthquakes in the Cook Inlet region and found spatial amplification variation dependent on source

1. Department of Earth and Environmental Sciences, San Diego State University, San Diego, California, U.S.A., https://orcid.org/0000-0002-9146-6804 (T-YY); https://orcid.org/0000-0002-3078-485X (KBO); 2. Department of Earth Sciences, University of Southern California, Los Angeles, California, U.S.A.; 3. Earth Research Institute, University of California Santa Barbara, Santa Barbara, California, U.S.A., https://orcid.org/0000-0003-0612-7654 (JHS); 4. Alaska Science Center, U.S. Geological Survey, Anchorage, Alaska, U.S.A., https://orcid.org/0000-0002-1503-6247 (PJH)

*Corresponding author: tyeh2@sdsu.edu

Cite this article as Yeh, T.-Y., K. B. Olsen, J. H. Steidl, and P. J. Haeussler (2025). Near-Surface Material and Topography Generate Anomalous High-Frequency Ground-Motion Amplification in Chugiak, Alaska, *Bull. Seismol. Soc. Am.* **115**, 2793–2808, doi: 10.1785/0120240283

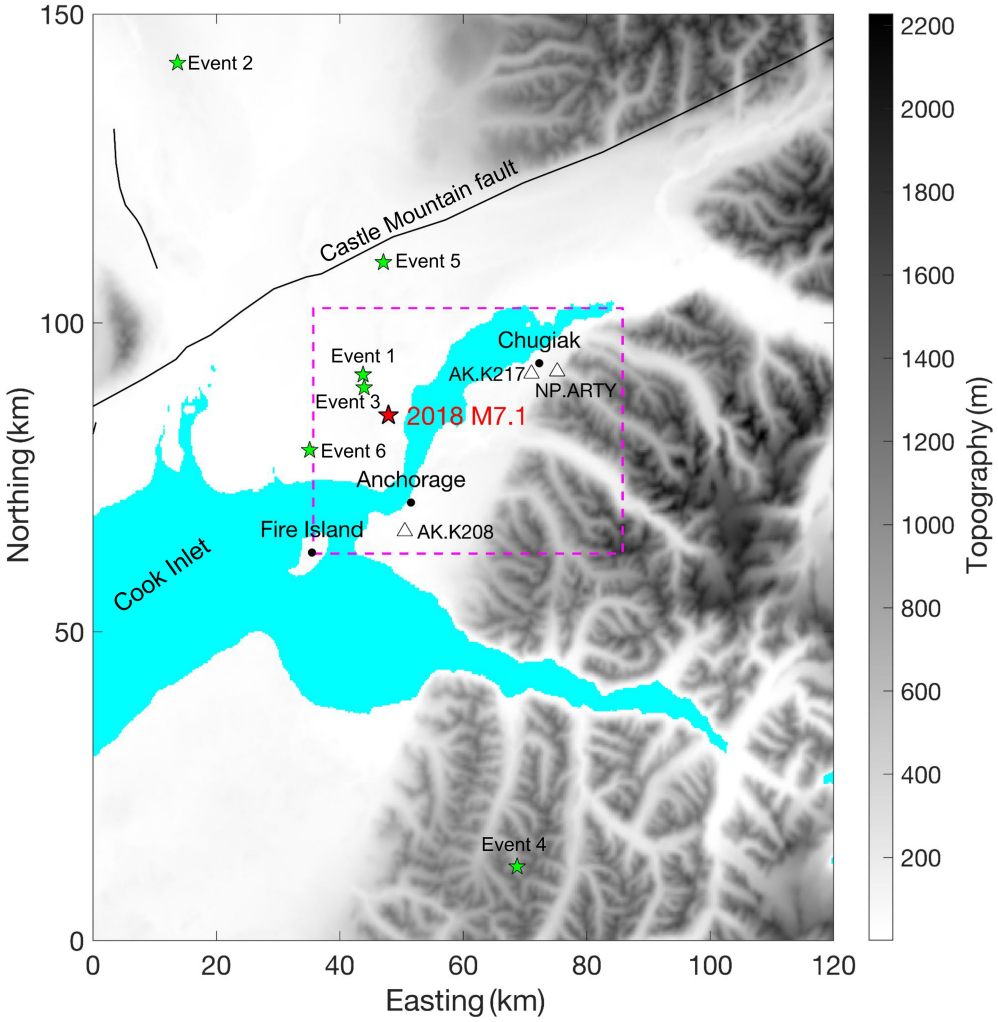

Figure 1. Map of study area with the dashed box depicting the simulation domain. Triangles show the locations of permanent stations, including NP.ARTY and two additional stations (AK.K217 and AK.K208) used for waveform comparisons in Figures 2 and 7. The red star depicts the hypocenter of the 2018 M_w 7.1 Anchorage earthquake. Green stars indicate the locations of select events that were well recorded by the U.S. Geological Survey (USGS) nodal array and were used for our analysis of seismic amplification along the nodal array. Shading depicts surface topography. The color version of this figure is available only in the electronic edition.

location and deviation in depth scaling of long-period basin amplification. These studies, mainly focused on seismic effects below about 4 Hz, suggest highly complex basin and regional amplification patterns. On the other hand, high-frequency seismic amplification is poorly constrained in the broader region in general, except for the well-instrumented areas within downtown Anchorage.

This study was motivated by the anomalously large ground motion (~2*g*) recorded at the NetQuake station NP.ARTY (Chugiak, AK) during the 2018 M_w 7.1 mainshock. Cramer and Jambo (2019) used ground-motion models (GMMs) to illustrate the extreme ground motion recorded at NP.ARTY appears to be an outlier whereas the majority of the other observations follow the GMMs reasonably well. In Figure 2, we compared the waveforms and the Fourier amplitude spectra (FAS) recorded at NP.ARTY (Peters Creek), AK.K217 (Chugiak Fire Station, 4 km west of NP.ARTY), and AK.K208 in downtown Anchorage (see Fig. 1 for location) during the 2018 M_w 7.1 Anchorage earthquake. The peak ground acceleration (PGA) value at NP.ARTY (1.98*g*) is about five times larger and in stark contrast to that recorded at AK.K217 despite the relatively short distance between the two stations. The recorded waveform amplitude level and spectra at AK.K217 are similar to those at stations in downtown Anchorage (see Fig. 2), except for an enrichment of long-period energy (<1 Hz) at AK.K208. The amplification leading to the large PGA at NP.ARTY is primarily associated with frequencies between 3 and 8 Hz. We note that NP.ARTY was bolted to the concrete slab (see picture in Fig. S1, available in the supplemental material to this article), without any sign of sliding movement during the strong ground shaking of the 2018 M_w 7.1 earthquake. Cramer and Jambo (2019) further pointed out the presence of till and glacial deposits underneath NP.ARTY, situated near a steep slope.

To better understand the reasons for the anomalously large ground motions recorded at NP.ARTY, the U.S. Geological Survey (USGS) deployed a ~3 km long pseudolinear nodal array with 80 nodes oriented approximately east–west and intersecting NP.ARTY, from 9 August 2021 to 8 September 2021 (see dots in Fig. 3a for locations). The topography and surficial geology along the transect are characterized by a series of flat surfaces and steep slopes, interpreted as kame terraces and outwash fans, which formed during deglaciation prior to 14 kya (Kopczynski *et al.*, 2017). The seismic recordings for a large number of aftershocks of the M_w 7.1 Anchorage earthquake obtained using the nodal array along with NP.ARTY provide an excellent dataset to analyze the causes of the anomalous amplification at NP.ARTY and the immediate surroundings.

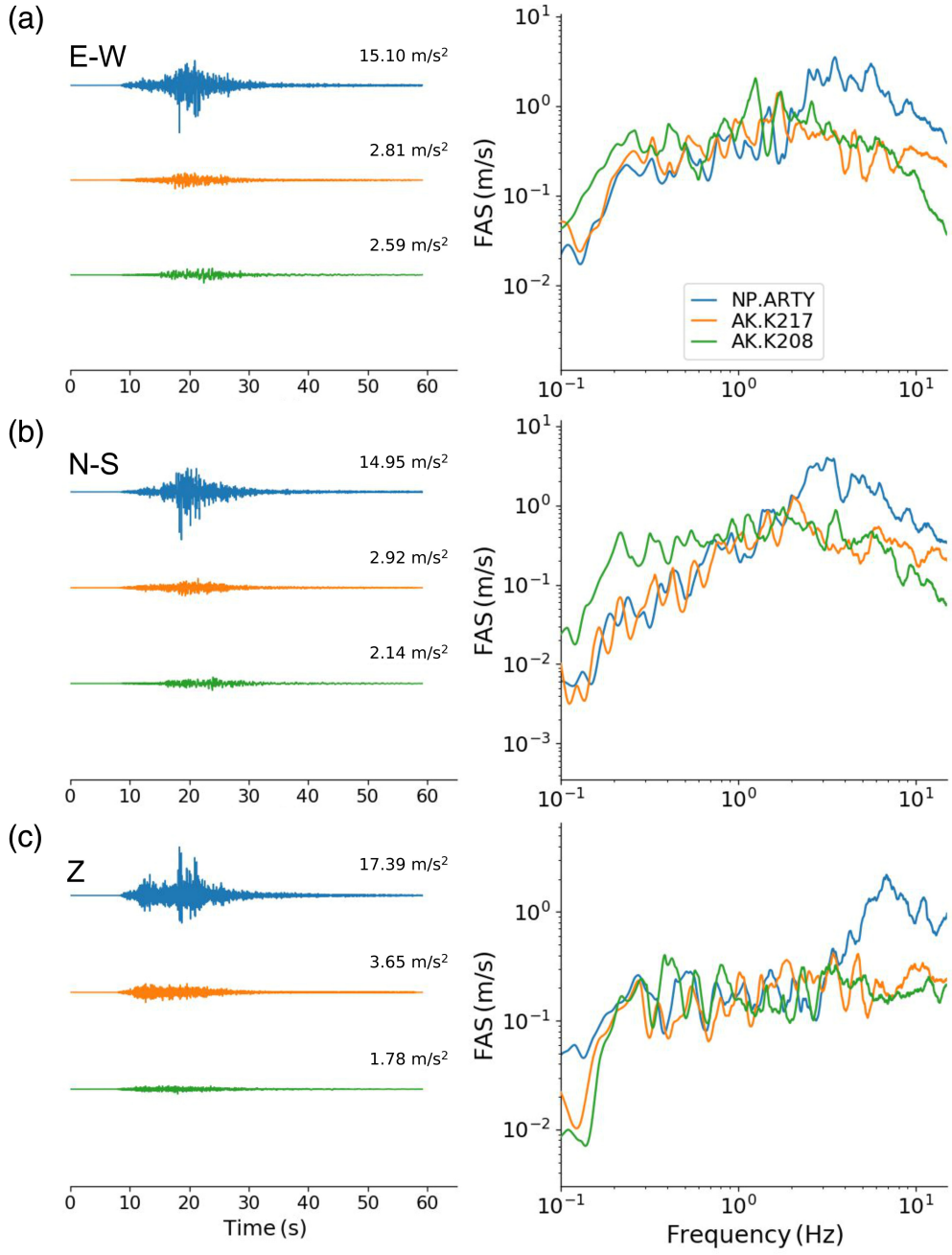

Figure 2. Comparison of observed 0.1–15 Hz acceleration waveforms (with peak absolute acceleration values listed by the traces) and Fourier amplitude spectra on (a) E–W, (b) N–S, and (c) vertical components, recorded from the 2018 M_w 7.1 Anchorage, Alaska, earthquake at NP.ARTY (Peters Creek), AK.K217 (Chugiak Fire Station, ~4 km west of NP.ARTY), and AK.K208 (downtown Anchorage). FAS, Fourier amplitude spectra. The color version of this figure is available only in the electronic edition.

Here, we used 0–10 Hz 3D physics-based simulations of aftershocks from the M_w 7.1 Anchorage earthquake to investigate the causes of the anomalously large PGA values recorded at NP.ARTY and along the nodal array deployed in Chugiak. The study is structured with (1) introduction of nodal array data used in this study, (2) discussion of observed amplification along the array, (3) validation of the regional velocity and attenuation models, (4) refinement of the local velocity model around NP.ARTY, (5) quantification of the contribution from different model components, and (6) discussion and conclusions.

ANALYSIS OF NODAL ARRAY DATA

The USGS deployed a nodal array around station NP.ARTY in August and September 2021. The high spatial resolution (~35 m spacing) of the nodal deployment allows for detailed observation of the amplification pattern along the array. These nodes are well suited to record aftershock data with a wide frequency range (see, e.g., Catchings *et al.*, 2020, for the 2019 Ridgecrest earthquake aftershock sequence as well as the studies that used the data set).

To analyze the ground-motion amplification along the nodal array, we first combined the FAS of the horizontal components,

$$\mathrm{FAS}_H(f) = \sqrt{0.5(\mathrm{FAS}_E(f)^2 + \mathrm{FAS}_N(f)^2)}, \quad (1)$$

in which $\mathrm{FAS}_E(f)$ and $\mathrm{FAS}_N(f)$ are the FAS values at frequency f on the east–west and north–south components, respectively, smoothed using a triangular window of a width of 0.75 Hz on a linear scale. We further summarized the spectral energy by computing the root mean square (rms) of $\mathrm{FAS}_H(f)$ within a given frequency band, hereafter denoted as rms_H. Using the rms_H values, we computed the amplification factors at the ith node (A_i) in terms of rms ratio as

$$A_i = \frac{\mathrm{rms}_{H,i}}{\mathrm{rms}_H^{\mathrm{ref}}}, \quad (2)$$

in which $\mathrm{rms}_H^{\mathrm{ref}}$ is the median of the rms_H values measured at the five nodes at the east end of the array (nodes BM01–BM05),

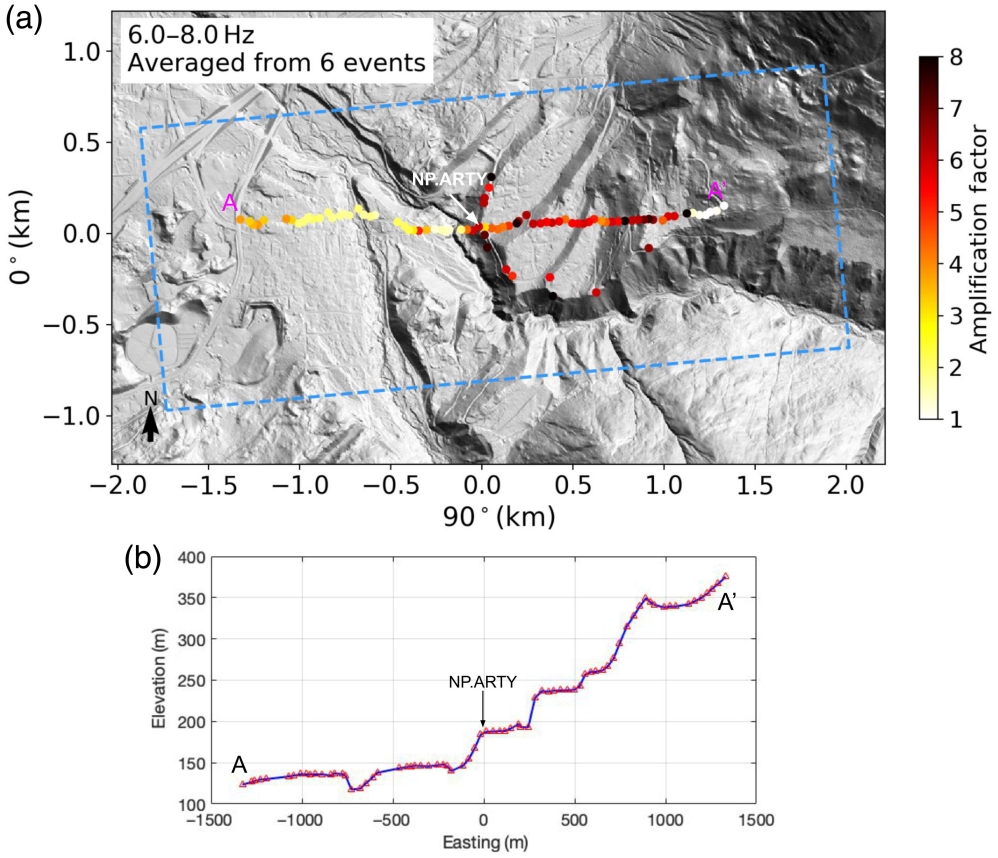

Figure 3. (a) Averaged rms_H (6–8 Hz) amplification factors along the nodal array across the six events shown in Figure 1. The dashed rectangle marks the boundary of the geologic map in Figure 4. (b) Elevation of nodes along the array (from A to A′). Note that the permanent station NP.ARTY is set to be the origin of the map, which is near the center of the array (0 m easting), as indicated by the black and white arrows. See comparisons for additional frequency bands in Figure S5. The color version of this figure is available only in the electronic edition.

for which ground motions appear to be constantly minimal. Given that this is different from the conventional approach for analysis of seismic amplification (e.g., Thornley *et al.*, 2022), we note that the goal of computing the rms ratio (equation 2) is to quantify how much larger the spectral energy is within a passband with respect to where the amplification is minimal (reference sites) as an effective way to demonstrate seismic amplification along the nodal array.

We computed A_i in four frequency bands to illustrate the seismic amplification along the array at various frequencies (2–4, 4–6, 6–8, and 8–10 Hz). Figure 3a shows averaged 6–8 Hz rms_H ratios (A_i) over 6 M_L 1.8–4.3 aftershocks (see Fig. 1 for event locations, and Table 1 for more details) from the M_w 7.1 Anchorage earthquake recorded by the nodal array, derived from analyzing a 20 s long window starting 5 s prior to the *P*-wave arrival for each event. Amplifications along the array for each individual event (see Figs. S2–S4) demonstrate patterns similar to that for the event-averaged values shown in Figure 3a. Additional comparisons of event-averaged amplification along the array shown in Figure S5 reveal that magnitude and pattern of seismic amplification can vary with frequency range. For instance, amplification pattern tends to be more localized at lower frequencies (see 2–4 Hz in Fig. S5a).

The averaged 6–8 Hz rms_H ratios (Fig. 3a) show amplification of 6–8 times the reference value along an about 1 km stretch of the array immediately east of station NP.ARTY and moderate amplification along the westernmost end of

TABLE 1
List of Events Used to Compute the Amplification Factor Shown in Figure 1 (Events 1–6) and Figure 5 (Events A1–A3)

Event Number	Event ID	Date (yyyy/mm/dd)	Location (Longitude/Latitude/Depth)	Magnitude	Nodal Array Data
1	ak021aah4ztg	2021/08/12	−150.026°/61.407°/44.0 km	M_L 2.2	Y
2	ak021aak1945	2021/08/12	−150.553°/61.870°/59.7 km	M_L 4.3	Y
3	ak021akofycq	2021/08/18	−150.025°/61.388°/45.9 km	M_L 1.8	Y
4	ak021anqhb9z	2021/08/20	−149.636°/60.682°/29.7 km	M_L 2.9	Y
5	ak021be8z840	2021/09/05	−149.948°/61.568°/40.2 km	M_L 3.1	Y
6	ak021bfvzqwd	2021/09/06	−150.198°/61.300°/48.3 km	M_L 2.3	Y
A1	ak018fe476ty	2018/12/01	−149.978°/61.376°/44.8 km	M_w 4.6	N
A2	ak20453123	2018/12/06	−149.955°/61.341°/43.2 km	M_w 4.8	N
A3	ak0215dsbmgn	2021/04/27	−149.980°/61.342°/43.8 km	M_w 4.8	N

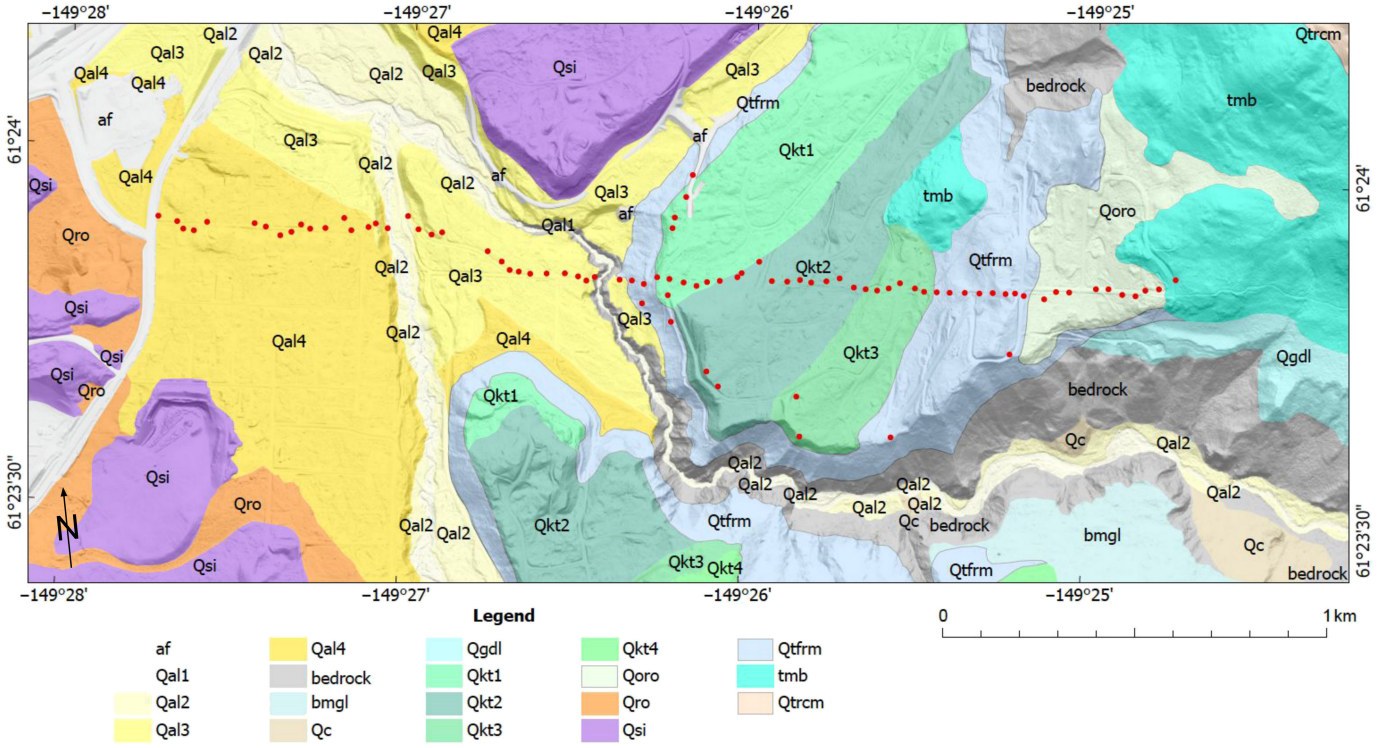

Figure 4. Quaternary geologic map for areas surrounding the nodal array, compiled from local surveys and the results from prior studies (Schmoll *et al.*, 1999; Kopczynski *et al.*, 2017). Red dots show locations of nodal stations deployed by USGS. The legend and description for the unit symbols can be found in Table S1. The color version of this figure is available only in the electronic edition.

the array (~4 times the reference value). In contrast, the nodes within about 1 km to the west of NP.ARTY show relatively low amplification (generally about two times or less relative to the reference stations).

NP.ARTY is installed in the garage of a single-family home in Chugiak, bolted to the foundation. Thus, it is reasonable to consider whether the large amplification recorded at NP.ARTY was affected by the building structure (e.g., "cavity effects," see Kroner *et al.*, 2005). However, the similarity in waveforms and FAS recorded at NP.ARTY and the closest node (BM41, ~40 m from NP.ARTY) for the 12 August 2021 aftershock (event 1) suggests that effects of the building on the amplification are minimal, and that the seismic response of NP.ARTY has been consistently captured by the nodal array (Fig. S6). In contrast, the amplitude level at the node located toward the eastern end of the array (BM01, a bedrock site) is much weaker. Thus, the nodal array data from the aftershocks not only agree with the anomalously strong ground motions recorded at NP.ARTY but also reveal additional sites encountering strong amplification along the array.

To better understand the relationship between local shallow geological units and the observed amplification pattern along the nodal array, we conducted a local field survey as a key component of this study, resulting in a detailed map of Quaternary geological units, shown in Figure 4. Cross comparison of Figures 3a and 4 indicates that the strong seismic amplification factors depicted in Figure 3a are primarily associated with the kame terraces (Qkt) and the Fort Richardson Moraine (Qtfrm) units (see Table S1 for more details). To explore such connection, we categorized the sites into two types in the following analyses, namely (1) type A sites, located outside Qkt and Qtfrm units where nodes consistently record relatively weak motions (factor of 3 amplification or smaller) and (2) type B sites, located within the Qkt and Qtfrm units that tend to experience relatively large motions (factor of 3 amplification or larger). In the following, we will demonstrate how we incorporated the local geological constraints (Fig. 4) into a 3D seismic velocity model of the Chugiak area and investigated the cause of the strong amplification observed at type B sites using 3D numerical wave propagation simulations. Specifically, we analyzed the relative contributions to the amplification from the deeper 3D structure, the near-surface low-velocity material, an additional shallow, constant-velocity near-surface layer, and surface topography.

NUMERICAL METHOD

To investigate the causes of the strong seismic amplification observed in Chugiak, Alaska, we performed 0–10 Hz 3D physics-based wave propagation simulations in a domain approximately 50 km (east–west) × 40 km (north–south) in size, covering the majority of Anchorage as well as the area near the permanent station NP.ARTY (dashed box in Fig. 1). We

used the anelastic wave propagation code AWP-ODC (with suffix from the authors Olsen, Day, and Cui). AWP-ODC is a fourth-order staggered-grid finite-difference code, which is graphic processing unit-enabled and highly scalable (Olsen, 1994; Cui *et al.*, 2013). AWP-ODC supports topography using a curvilinear grid (O'Reilly *et al.*, 2021), incorporated in the simulations using the USGS 5 m resolution digital elevation model (DEM) for the majority of the domain. The exception is the immediate area around NP.ARTY where we incorporate a 1 m resolution DEM from light detection and ranging (U.S. Geological Survey, 2020) to obtain increased resolution. The discontinuous mesh feature (Nie *et al.*, 2017) was adopted to reduce computational burden, for which the mesh was divided vertically into three mesh blocks with a factor of 3 increase in grid spacing. To resolve the simulated seismic wavefield up to 10 Hz, we used a grid spacing of 4 m with a minimum shear-wave speed of 250 m/s, maintaining a numerical accuracy of 6.25 points per minimum shear-wave length (O'Reilly *et al.*, 2021). We linearly interpolated DEMs with different resolutions onto the horizontal locations of the curvilinear grid at a resolution of 4 m.

AWP-ODC supports frequency-dependent anelastic seismic attenuation (Withers *et al.*, 2015) formulated as

$$Q_S(f) = Q_{S,0}, \qquad f < f_0$$
$$Q_S(f) = Q_{S,0}\left(\frac{f}{f_0}\right)^{\gamma}, \qquad f \geq f_0, \tag{3}$$

in which $Q_{S,0}$ is the low-frequency (constant) Q, f_0 is the transition frequency (here, 1 Hz following Withers *et al.*, 2015), and γ is the power-law exponent controlling the rate of increase at frequencies above f_0. We assumed $Q_P = 2Q_S$ and a linear relation between $Q_{S,0}$ and local V_S as $\frac{Q_{S,0}}{V_S} = k$, in which k is a constant (Olsen *et al.*, 2003). Table 2 lists the simulation parameters.

TABLE 2
Simulation Parameters

Domain	**Value**
Length	50.1 km
Width	39.7 km
Depth	59.9 km
Southwest corner	−150.2000°,61.1500°
Northwest corner	−150.1680°,61.5063°
Southeast corner	−149.2710°,61.1276°
Northeast corner	−149.2284°,61.4836°
Geodetic datum	WGS84
UTM zone	5
Spatial Resolution	
Maximum frequency	10 Hz
Minimum V_S	250 m/s
Points per minimum wavelength	6.25
Grid spacing	4 m: free surface to 5.50 km below the sea level 12 m: 5.47–6.99 km below the sea level 36 m: 6.91–59.9 km below the sea level
Temporal Resolution	
Timestep	0.00025 s
Simulation time	30 s

VELOCITY AND ANELASTIC ATTENUATION MODELS

Because no comprehensive community velocity model that includes detailed near-surface and basin structures is available for our area of interest, we started out with building the 3D numerical model for our simulations from scratch. A number of regional tomographic models are available for our area of interest (e.g., Eberhart-Phillips *et al.*, 2006; Wang and Tape, 2014; Ward, 2015; Martin-Short *et al.*, 2018; Ward and Lin, 2018; Berg *et al.*, 2020; Nayak *et al.*, 2020). We proceeded with *P*- (V_P), *S*-wave (V_S), and density information from the 3D model derived from the joint inversion of phase velocity measured from ambient noise cross correlation, Rayleigh-wave ellipticity, and receiver functions by Berg *et al.* (2020). However, the spatial resolution of the tomographic models is too coarse to provide sufficient details of sedimentary basin structures such as the boundary and low-velocity material of the Cook Inlet basin. To improve the description of the basin, we manually incorporated the structure of the Cook Inlet basin using the depth of the Mesozoic unconformity (Shellenbaum *et al.*, 2010) as the bottom of the basin, following the previous numerical studies in the same region (Grapenthin *et al.*, 2018; Silwal *et al.*, 2018). The generic basin V_S profile from Brocher (2008) was used to describe the elastic properties inside the basin, in which the V_S profile solely depends on depth (see Text S1 for more details about implementing the basin structure). Figure 5 compares V_S at the free surface of the model before and after implementing the basin structure, illustrating the much lower V_S in the Cook Inlet basin using the profile of Brocher (2008).

We calibrated the region-dependent attenuation parameters using simulations of three well-recorded M_w 4.6–4.8 aftershocks of the M_w 7.1 Anchorage earthquake (see Fig. 5b and events A1–A3 in Table 1). For the calibration, we used strong-motion data from the Center for Engineering Strong Motion (CESMD), including stations within the NP (U.S. Geological Survey, 1931) and AK (Alaska Earthquake Center, Univ. of Alaska Fairbanks, 1987) networks that are located inside the simulation domain (triangles in Fig. 5).

We simulated wave propagation for the three aftershocks using point sources (see Text S2 for source description). By computing the simulation-to-observation FAS ratio, we quantified model bias at different frequencies ε as

$$\varepsilon(f) = \log_{10}\left(\frac{\mathrm{FAS}_{\mathrm{model}}(f)}{\mathrm{FAS}_{\mathrm{data}}(f)}\right), \tag{4}$$

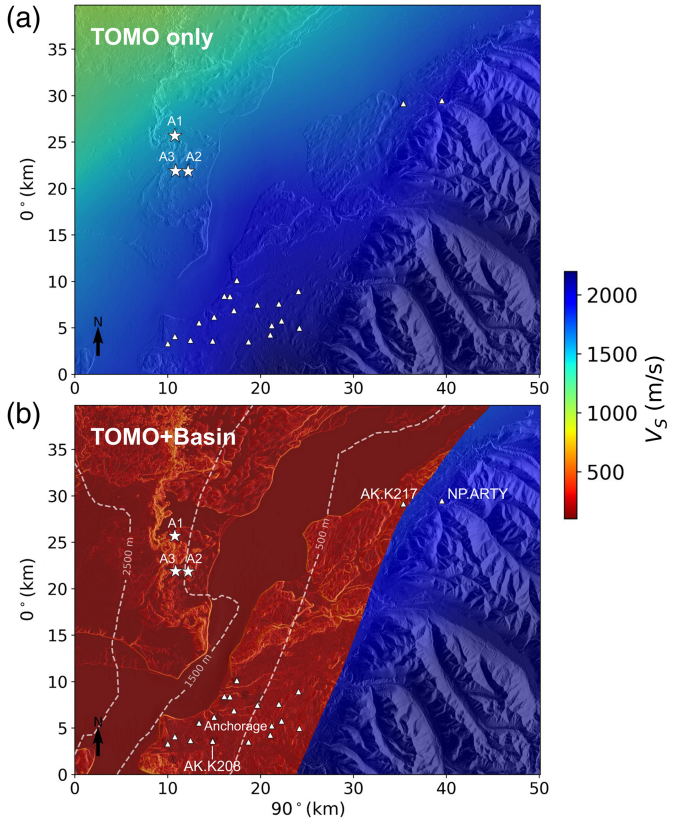

Figure 5. Surface V_S within the simulation domain with the 3D tomography model from Berg *et al.* (2020) (a) in its original form and (b) modified to include velocity and density values for generic basins from Brocher (2008). White triangles are locations of strong-motion stations used for calibration of attenuation model parameters. Stars depict locations of the three M_w 4.6–4.8 events used for calibration of the attenuation model (events A1–A3 in Table 1). Dashed lines are contours of basin depth from Shellenbaum *et al.* (2010). The color version of this figure is available only in the electronic edition.

in which $\mathrm{FAS}_{\mathrm{model}}(f)$ and $\mathrm{FAS}_{\mathrm{data}}(f)$ are the FAS of simulated and observed waveforms, respectively, smoothed using a triangular window of a width of 0.75 Hz.

We calculated the mean FAS bias curve (equation 4) over a total of 46 recordings for the three events to quantify the overall performance of different seismic attenuation models at each frequency point. We note that station NP.ARTY was excluded in this analysis to avoid bias due to the unmodeled anomalously large amplification. The absolute values of all points along the mean FAS bias curves across all three components were averaged as a single-value metric of model performance, which we refer to as the FAS error from here on, given by

$$\mathrm{Err}_{\mathrm{FAS}} = \frac{\sum_{i=1}^{i=N_f} |\varepsilon_i|}{N_f}, \tag{5}$$

in which N_f is the number of frequency points across all three components.

The optimal values for our frequency-dependent seismic attenuation model parameters, k and γ, were determined by minimizing $\mathrm{Err}_{\mathrm{FAS}}$ via grid search within [0.05,0.15] for k with a step size of 0.025 and within [0,0.4] for γ with a step size of 0.2. Based on the $\mathrm{Err}_{\mathrm{FAS}}$ values computed from 36 sets of three-component recordings at 19 stations (Fig. 5) across the three validation events (events A1–A3), we found optimal values of γ of [0,0.2] and k = 0.125 (Fig. S8a).

We found that $\gamma = 0$ performs better on the horizontal components while underpredicting on the vertical component; $\gamma = 0.2$ provides a better fit on the vertical component with slight overpredictions on the horizontal components at frequencies above 7 Hz (see Fig. S8b). Further optimization of γ within the 0–0.2 range was carried out via simulations of the nodal array data, discussed later in the Implementation of Near-Surface LVT section.

By optimizing the seismic attenuation parameters, we aimed to reduce prediction bias and better utilize the available velocity model. The resulting simulated ground motions show generally acceptable agreement with observations across the frequency range of interest. Figure 5 shows that the strong-motion stations used for the model calibration are inside the city of Anchorage, except for AK.K217 at Chugiak Fire Station (NP.ARTY excluded from this analysis). Figure 6 shows the contribution of the included basin model, reducing $\mathrm{Err}_{\mathrm{FAS}}$ by 73% from the model excluding the basin structure. Comparison of simulated and observed waveforms for the 2018 M_w 4.6 event (event A1 in Table 1) at AK.K208 in downtown Anchorage as well as at AK.K217 and NP.ARTY (see Fig. 7) demonstrates that the simulation with the calibrated attenuation model underpredicts acceleration waveforms at NP.ARTY, whereas those at AK.K208 and AK.K217 are simulated reasonably accurately when the structure of Cook Inlet basin is included. On the other hand, it is clear that the geometric effects of topography alone cannot explain the large amplification at NP.ARTY. Despite the close proximity of AK.K217 and NP.ARTY (~4 km), AK.K217 is located within the Cook Inlet basin with the presence of low-velocity material at shallow depths (V_S of 250–750 m/s in the top 50 m) after incorporating the basin structure, whereas NP.ARTY is outside the basin with relatively high-V_S values (1850–2000 m/s) in the top 50 m. Thus, the simulations presented so far suggest that the amplification at NP.ARTY may be caused by near-surface V_S values that are likely much lower than those in the 3D tomography model. Our next step is therefore to propose and test refined velocity models to reproduce the recorded strong ground motions near NP.ARTY, considering the local geology information.

SIMULATION OF SEISMIC AMPLIFICATION ALONG THE NODAL ARRAY

With the small spacing between nodes (~35 m), the nodal array provides high-resolution observations of the seismic

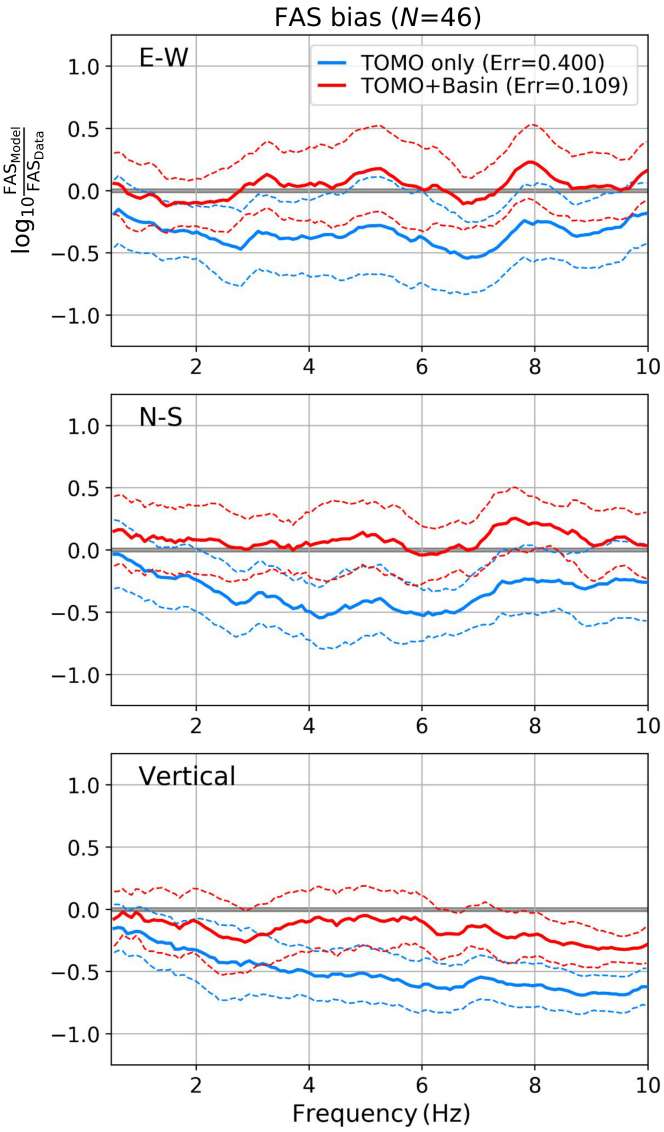

Figure 6. Averaged FAS bias computed from 46 sets of three-component recordings for the three validation events (events A1–A3 in Table 1) at stations shown in Figure 5 (excluding NP.ARTY) for a model with (blue) the 3D tomography model by Berg *et al.* (2020) only and (red) the modified model including the basin structure. Both models are computed using the preferred attenuation model with $Q_S = 0.125V_S$ and $\gamma = 0$. Dashed curves depict the standard deviation. The color version of this figure is available only in the electronic edition.

amplification along the array. The most straightforward approach to analyze the cause of strong amplification is to simulate the ground motions recorded by the nodal array. Unfortunately, no moment tensor solution is available for the recorded events due to the small magnitudes. As a work around, we chose an aftershock well recorded by the nodal array (event 1, M_L 2.2) that is in close proximity to one of the three selected events used for the calibration of the attenuation model (event A1, M_w 4.6) and assumed the same focal mechanism (see Fig. 1, and Table 1 for locations and details). This was accomplished by scaling down the moment tensor components of event A1 to match the seismic moment of the simulated event (event 1). We adopted a minimum phase moment rate function for event 1, in which the Fourier amplitude spectrum has an omega-squared fall-off with a characteristic time controlling the width of the pulse of $T_c = 0.0087$ s, assuming an M_w of 2.2 (also see Text S2 for source description).

Implementation of near-surface LVT

Outside of the Cook Inlet basin, the V_S values in the Berg *et al.* (2020) 3D model around the nodal array are relatively high near the surface (1800–2000 m/s, see Fig. 5) due to limited resolution of the regional tomography model. Unrealistically high-V_S values at shallow depths have been shown to result in underprediction near NP.ARTY. To refine the near-surface velocity structure, we first implemented a low-velocity taper (LVT) to better describe the shallow seismic structure in the area. The implementation of the LVT replaces the near-surface velocity and density structures with a tapered profile to lower the shallow velocities considering the local V_{S30} information, along with a smooth transition into the original model at the bottom of the taper (i.e., tapering depth or z_T). See Text S3 for more details about implementation of the LVT.

In the anticipation of a trade-off between LVT and anelastic parameters, we simultaneously determined the optimal values of z_T and γ by trial-and-error for the area around the nodal array. We found the best fit at $\gamma = 0.2$, whereas $\gamma = 0$ generally leads to slight underprediction along the nodal array. The FAS bias curves for various z_T (Fig. 8) indicate an optimal fit for a tapering depth of about 300 m. We note that the 300 m tapering depth generates an FAS bias that approaches zero at type A sites on all three components (Fig. 8a), whereas type B sites are still significantly underpredicted (Fig. 8b). With the LVT of a 300 m tapering depth, $\mathrm{Err}_{\mathrm{FAS}}$ is reduced by 79% and 54% for type A and type B sites, respectively, relative to the model without the LVT. The results suggest that while significantly reducing the bias, implementing the LVT is still not sufficient to produce the observed amplification at type B sites, calling for additional improvements on the velocity structure. Because the recorded ground motions at type A sites are simulated reasonably well using the LVT alone, the velocity structure beneath type A sites will remain unchanged from here on.

FURTHER REFINEMENT OF THE NEAR-SURFACE MODEL

To further improve the velocity model beneath type B sites, we incorporated information from the Quaternary geologic map of the area (Fig. 4) into our 3D velocity model. The geologic map reveals that the nodes that recorded elevated ground motions are primarily located on till (Qtfrm) and kame terrace (Qkt1, Qkt2, and Qkt3) units. The kame terraces sit on top of a thick, widespread till unit with underlying bedrock (Fig. 4). To incorporate these two units into the velocity model, we first added the till unit, replacing the shallowest part of the LVT. Here, we used local

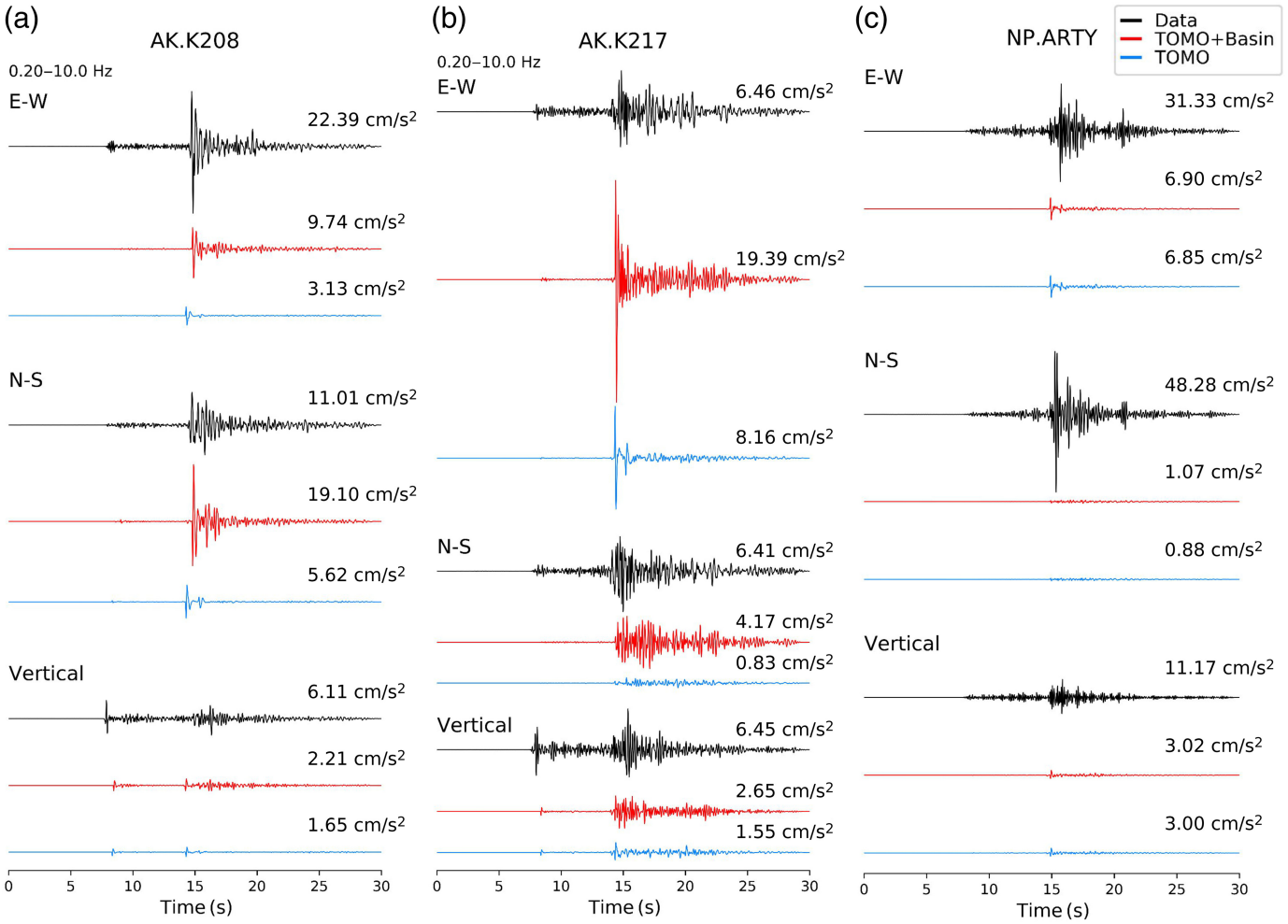

Figure 7. Comparison of observed and simulated acceleration waveforms computed using the calibrated attenuation model ($Q_S = 0.125V_S$ and $\gamma = 0$) (red) with and (blue) without the Cook Inlet basin structure added at stations (a) AK.K208 in Anchorage, (b) AK.K217 at Chugiak Fire Station, and (c) NP.ARTY at Peters Creek for the M_w 4.6 event (event A1 in Table 1). Severe underprediction at NP.ARTY motivates further refinement of the near-surface velocity structure. See Figure 1 for station locations. The color version of this figure is available only in the electronic edition.

water well log records (Alaska Department of Natural Resources - Information Resource Management, 2013) to obtain depth to bedrock information (see data points in Fig. S9), which was interpolated using distance weighting and used as a constraint on the thickness of the till unit (Fig. 9a). We used the generic profile for rock sites from Boore and Joyner (1997), rescaled to match a V_{S30} of 400 m/s to describe the V_S profile of the till unit. The kame terraces were then added by replacing the shallowest part of the till unit, as guided by the geologic map (Fig. 4). However, neither the thickness nor the seismic velocity of the kame terrace units are well constrained. For this reason, we tested different thicknesses with a V_S of 250 m/s for the kame terrace units, and we narrowed down the range for the optimal thickness to roughly between 4 and 8 m (Fig. S10). Given the strong amplification between 6 and 10 Hz in the recordings, we proceeded with a thickness of 8 m for the kame terrace units (Fig. 9c), which is expected to results in a 1D fundamental resonance *S*-wave frequency (f_0) of ~8 Hz, estimated using $f_0 = \frac{V_S}{4H}$, in which H is the thickness of the layer. The addition of these two units creates a low-velocity layer along with a sharp contrast across the bottom boundary of the till unit (Fig. 9b), promoting amplification and entrapment of waves, in contrast to the gradual change in impedance when implementing the LVT alone.

Simulation results indeed show that including the till and kame units to the model significantly enhances the wave energy at type B sites in the simulations over the 2–10 Hz band, moving the mean FAS bias curve much closer to zero (see Fig. 10). Specifically, the three-component combined $\mathrm{Err}_{\mathrm{FAS}}$ at type B sites is reduced by 63% from the model with LVT only (Fig. 10b). To demonstrate the improvement at various frequency ranges, we compared the observed and model predicted rms_H within narrow frequency bands along the nodal array (see top panels in Fig. 11a,b). These comparisons show that the amplification effects from the local low-velocity units (kame terraces and till) are essential to match the observations at type B sites for both lower (2–4 Hz) and higher (6–8 Hz) frequency bands, whereas type A sites can be well modeled

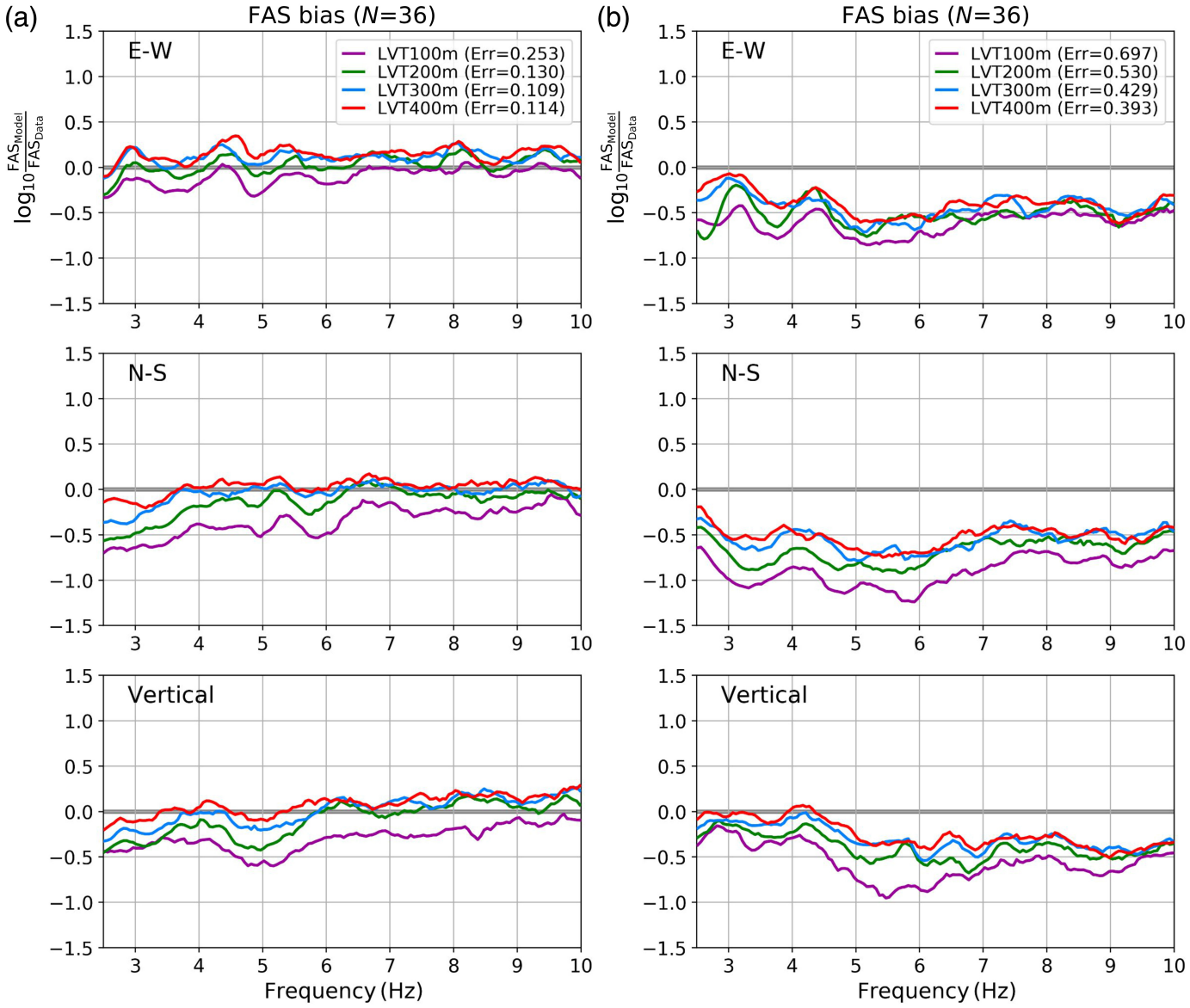

Figure 8. Comparison of the mean FAS bias curves for (a) type A and (b) type B sites along the nodal array for the event 1 (see Fig. 1), corresponding to simulations with LVT tapering depths of 100 m (purple), 200 m (green), 300 m (blue), and 400 m (red). $\gamma = 0.2$ is used in these simulations. The number of recordings for calculating the FAS bias for each site type is shown at the top of the panel. Error values shown in the legend are the mean absolute FAS bias over three components. The color version of this figure is available only in the electronic edition.

by only using the LVT. Comparison for additional frequency bands can be found in Figures S11 and S12. Comparison of waveforms and spectra at node BM41, located 40 m to the northwest of NP.ARTY, reveals that the inclusion of the kame terrace and till units in the model is critical to match the wave energy on the north–south and vertical components of the observation (Fig. 12).

TOPOGRAPHIC AMPLIFICATION ALONG THE NODAL ARRAY

The seismic amplification along the nodal array generated in the simulations includes the combined effects of the topography and the local geologic units. Attempting to fairly quantify the impact of the topography on the local wavefield, we built a numerical mesh with a flat free surface by "squashing" the material above sea level. The "squashed" model, as demonstrated in Aagaard *et al.* (2008), was built by vertically shifting the elastic properties at each horizontal grid location by the local topographic elevation value to align with sea level, which preserved the depth dependence of all seismic structures (compare Fig. 9b to Fig. 9d). For the model with a flat free surface, the three-component combined $\mathrm{Err}_{\mathrm{FAS}}$ is 1.5–1.8 times higher than the value computed from the model with DEM topography (Fig. 10), representing the amplification effects from the latter. The effects of surface topography are more profound on the north–south and the vertical components, generating stronger and longer coda-wave trains caused by additional seismic scattering near the free surface.

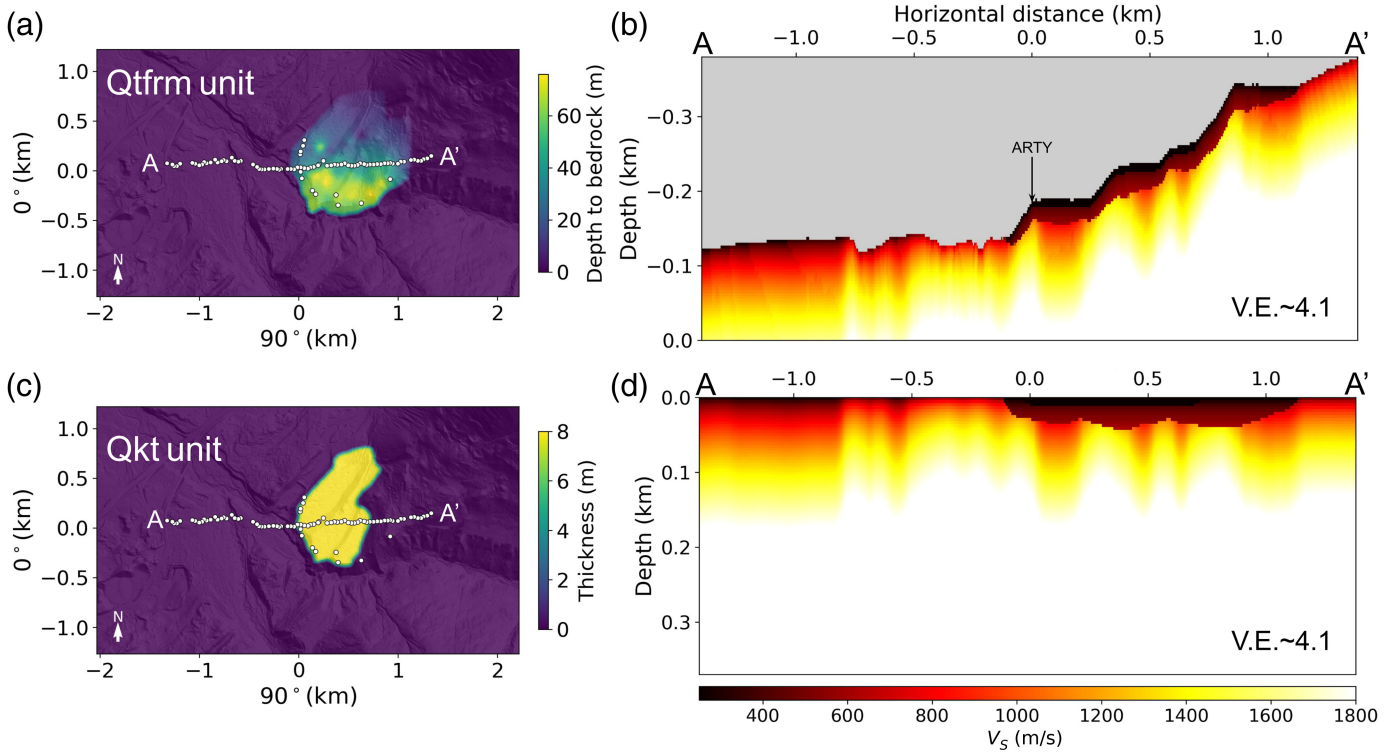

Figure 9. (a) Map of the depth to bedrock around the USGS array, obtained from water well logging data, and used as a proxy for the thickness of the till unit. (b) V_S transect along the nodal array (A–A′ profile, see Fig. 3a for location) for the simulation including topography, a 300 m thick LVT, till, and kame terraces. (c) Estimated thickness map of the kame terrace units. (d) Same velocity structure as panel (b), but "squashed" to the sea level to represent a flat surface. The origin of maps in panels (a) and (c) corresponds to the location of the permanent station NP.ARTY, which is the same as the x axis in panels (b) and (d). White dots in panels (a) and (c) depict the locations of nodes in the USGS array. The transects are vertically exaggerated (V.E.) by a factor of ~4.1. The color version of this figure is available only in the electronic edition.

The second row of panels in Figure 11a,b quantifies and highlights the amplification from surface topography along the nodal array for passbands of 2–4 and 6–8 Hz, defined in terms of logarithmic ratio

$$\log_{10}\frac{\mathrm{rms}_H^{\mathrm{Topo}}}{\mathrm{rms}_H^{\mathrm{Flat}}}, \tag{6}$$

in which $\mathrm{rms}_H^{\mathrm{Topo}}$ and $\mathrm{rms}_H^{\mathrm{Flat}}$ are root mean squared FAS_H (equation 1) values for models with DEM topography and a flat free surface, respectively. As expected, the higher frequency band (Fig. 11b) is associated with more complex topographic amplification patterns than the lower frequency band (Fig. 11a). The strongest topographic amplification (more than 200% at around 6 Hz) is found near the western edge of and inside the bowl-shaped area within x= [800, 1000 m] (see node BM14 in Fig. 11 and Fig. S13d), likely caused in part by geometrical focusing and wave entrapment in the near-surface deposits. Similar amplification can be observed near nodes BM40 (x = 0 m), BM31 (x = 350 m), BM23 (x = 600 m), and BM14 (x = 950 m; see Fig. 11 and Fig. S13). Our result suggests that the magnitude of topographic amplification is strongly frequency dependent (Fig. S13) but generally more profound at lower frequencies (below 6 Hz). We note that the frequency dependence of the topographic scattering is likely in part affected by the variation of the near-surface material, as pointed out by Mohammadi and Asimaki (2017).

Our results show that topography is capable of increasing the overall rms_H values across various frequency bands in units of the mean absolute percent difference for all type B sites by 40% and 33% within passbands 2–4 and 6–8 Hz, respectively. In contrast, the seismic amplifications caused by the inclusion of the kame terrace and till units (the model with tomography (TOMO) + LVT + Qt + Qkt relative to the model with TOMO + LVT only) are 204% and 139% within 2–4 and 6–8 Hz, respectively. The amplifications from the optimal LVT (TOMO + LVT vs. TOMO only) within 2–4 and 6–8 Hz are 179% and 272%, respectively. Thus, although all model features are shown to contribute to the seismic amplification, our results show that the LVT and the local near-surface geologic units cause much stronger effects on the ground motions at type B sites than the surface topography.

DISCUSSION AND CONCLUSIONS

We used 0–10 Hz physics-based simulations and ground-motion records from an aftershock of the 2018 M_w 7.1 Anchorage, Alaska, earthquake to explore the causes of anomalously large

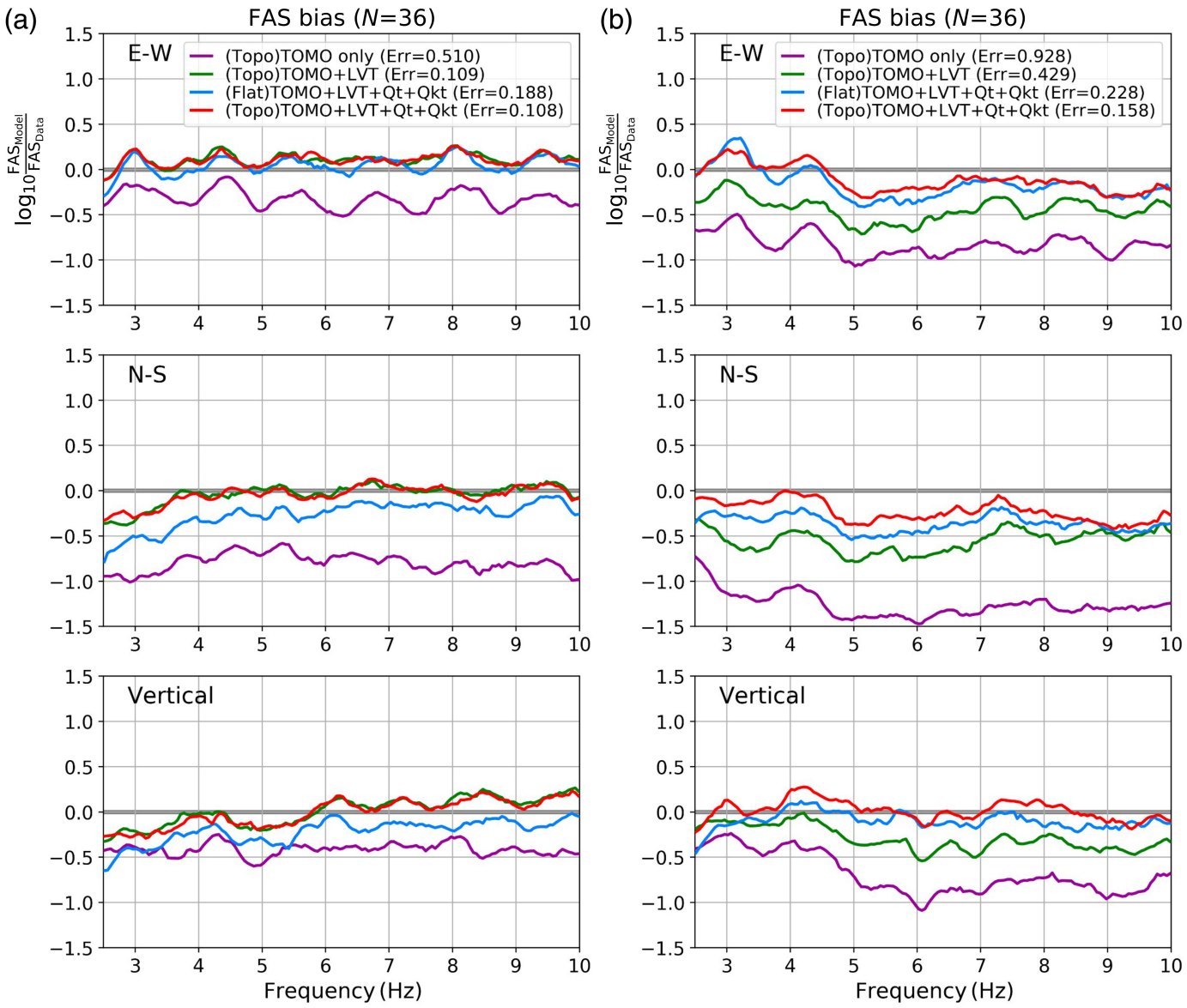

Figure 10. Comparison of the mean FAS bias curves for event 1 (see Fig. 1 and Table 1) computed for (a) type A and (b) type B sites along the nodal array; (purple) tomography (TOMO) only, (green) TOMO + LVT, (blue) TOMO + LVT + kame terraces and till (flat free surface), and (red) TOMO + LVT + kame terraces and till (high-resolution surface topography). The number of recordings for calculating the FAS bias for each site type is shown at the top of the panel (*N*). Bias error values shown in the legend are three-component mean absolute values. The color version of this figure is available only in the electronic edition.

PGA values recorded at permanent station NP.ARTY and a local nodal array in the Chugiak area, 30 km north of Anchorage. Using the regional 3D tomographic model from Berg *et al.* (2020) with the embedded basin structure of the Cook Inlet basin (Shellenbaum *et al.*, 2010) and our data-constrained attenuation parameters for the Cook Inlet basin of $Q_s(f) = 0.125V_S f^{0-0.2}$ (V_S in m/s), we quantified the amplification effects caused by surface topography via a high-resolution (1 m) DEM, LVT, and the local glacial units. Our results conclude that the unexpectedly large high-frequency amplification recorded in Chugiak is caused by a combination of topographic effects and the local near-surface low-velocity material, with (by far) larger contribution from the latter.

Our results show the effectiveness of minimizing the underprediction of ground-motion amplification by incorporating an LVT into a tomographic model with limited near-surface resolution. The optimal estimated tapering depth for the LVT is 300 m, which is substantially thinner than that estimated for Southern California (Hu *et al.*, 2022a,b; Yeh and Olsen, 2023, 2024). This is expected due to slower surface weathering in the Anchorage area as compared to Southern California. The estimated attenuation model for the Cook Inlet basin area, on the other hand, is similar to the estimation for Southern California (Hu *et al.*, 2022a,b; Yeh and Olsen, 2023).

The V_{S30} value of 400 m/s estimated for the till unit in this study is in general agreement with those measured at other

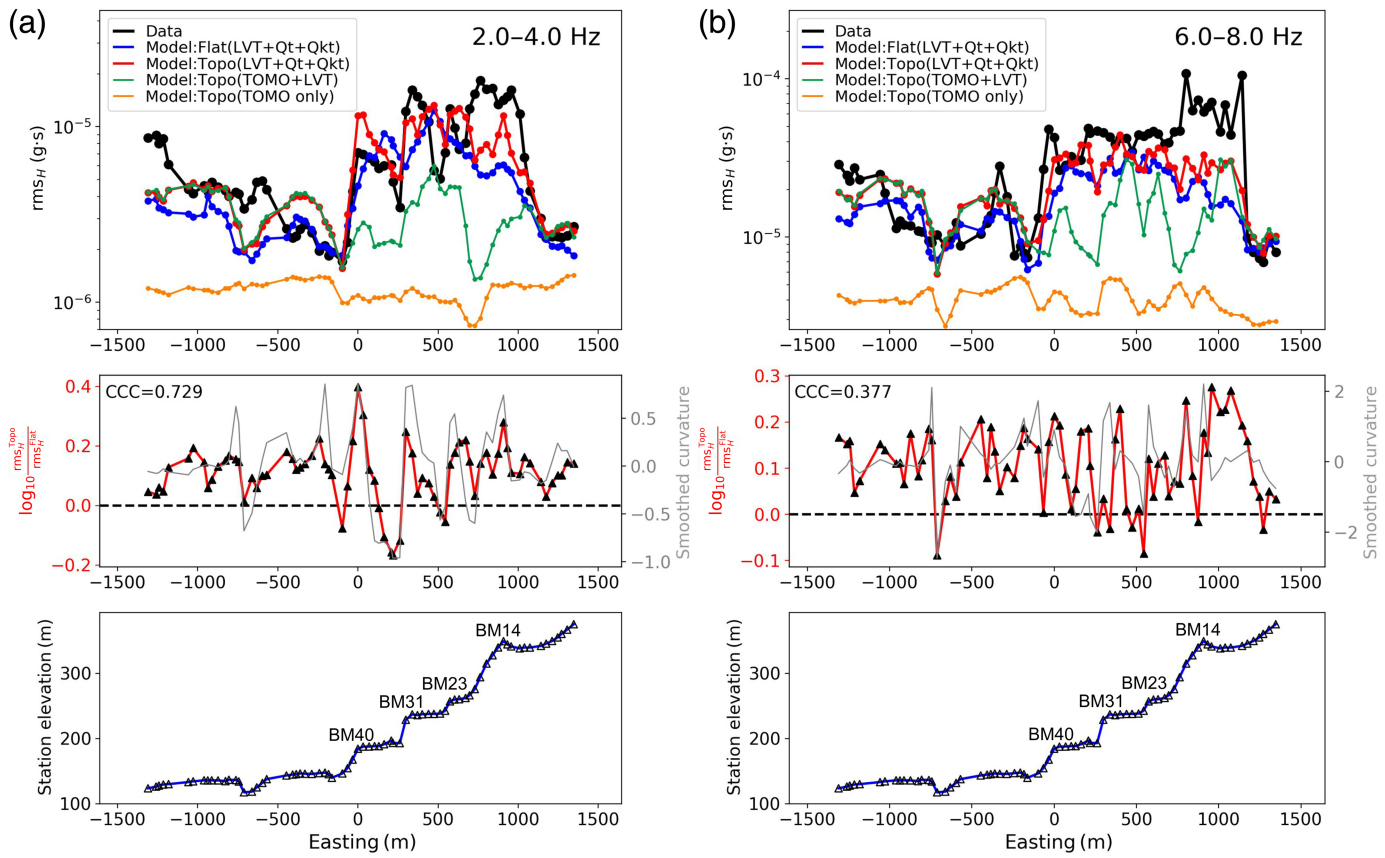

Figure 11. Comparison of root mean square (rms) FAS$_H$ (see equation 1) and the local topographic amplification (equation 6) values computed from the USGS nodal array recordings of the 12 August 2021 M_L 2.2 aftershock (event 1, also see Fig. 1) and simulations band-pass filtered to (a) 2–4 and (b) 6–8 Hz frequency bands. Comparisons for additional frequency bands can be found in Figures S9 and S10. The origin of the *x* axis corresponds to the location of the permanent station NP.ARTY. Topographic amplification values in the middle panels of (a) and (b) are superimposed with the curvature of the topography, smoothed using scale lengths of 113 and 48 m for the 2–4 and 6–8 Hz passbands, respectively (gray), calculated based on one-half of the *S*-wave wavelength (Maufroy *et al.*, 2015). The cross-correlation coefficient (CCC) values between the topographic amplification and the corresponding smoothed curvature are shown in the upper left corner. Bottom panels of (a) and (b) depict the elevation of the recording sites along the nodal array, with four node locations linked to larger positive topographic curvature values labeled. The color version of this figure is available only in the electronic edition.

sites with a similar geological setting (Dutta *et al.*, 2000). However, several parameters in our optimal crustal model of the Chugiak area are associated with considerable uncertainty, including the till units, and in particular, the kame terraces, which are mixed sediment units of diamict, silts, sands, and gravels. We note minor levels of underprediction by our simulations, the largest at the stations near the eastern end of the nodal array (x = [800, 1200 m], see Fig. 11a,b), which we attribute to oversimplification of the shallow structure of the till unit (Qtfrm). In addition, the simulated amplification factors along the nodal array match the observed values better within the 2–4 Hz band (Fig. S14) than within the 6–8 Hz band (Fig. S15). The reason for this is likely that the estimated values from our analysis (V_S of 250 m/s and a thickness of 8 m) may not be accurate for some sites along the nodal array for the kame terrace units and can be improved once more detailed seismic constraints are available. The presumed minimum shear-wave speed of 250 m/s required for the numerical accuracy also limits our ability to explore additional parameter combinations with lower V_S values for the kame terraces units.

Our results show that topographic amplification along the nodal array is highly frequency dependent. Such frequency dependence of topographic amplification was also demonstrated by Maufroy *et al.* (2015) using simple half-space models with irregular topography, showing that the curvature of realistic topography smoothed with length scales of approximately one-half the *S*-wave lengths correlates well with the resulting amplification. Here, we also examined this correlation along the nodal array in the middle panels of Figure 11a,b, using length scales of 113 m at 3 Hz (2–4 Hz) and 48 m at 7 Hz (6–8 Hz), assuming an averaged V_{S30} of 678 m/s along the nodal array. Following Maufroy *et al.* (2015), the length scales here refer to one-half of the shear wavelength ($0.5\frac{V_S}{f_b}$), in which f_b is the central frequency of each band. We found fairly high correlation between the smoothed curvature of the topography and the amplification at many nodal station locations particularly at lower frequencies (see 2–4 Hz band Fig. 11a). The

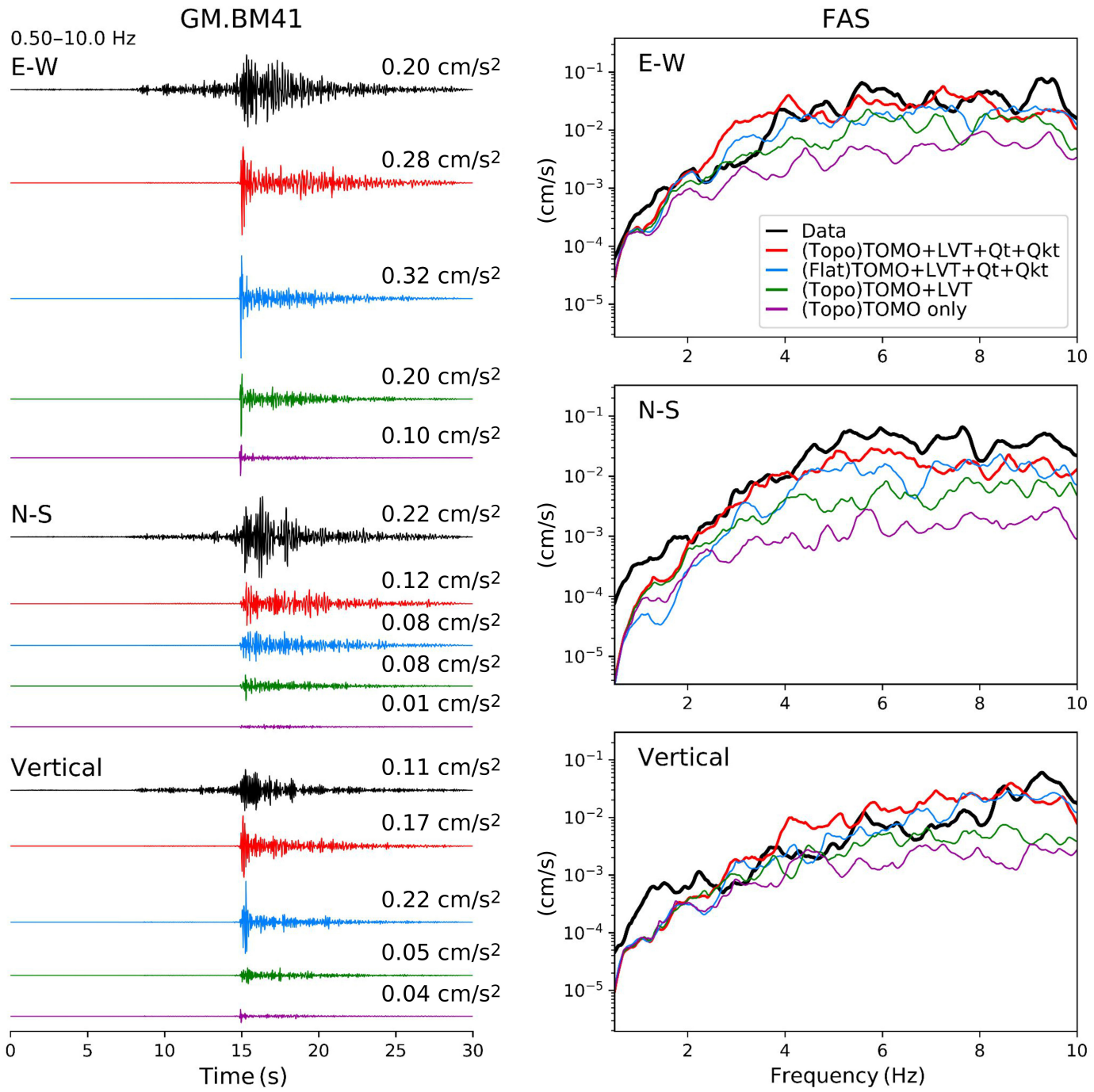

Figure 12. Comparison of waveforms and spectra for event 1 (see Fig. 1) at node BM41 (40 m from NP.ARTY) for recordings and a simulation with (red) TOMO + LVT + kame terraces and till (high-resolution surface topography), (blue) TOMO + LVT + kame terraces and till (flat free surface), (green) TOMO + LVT, and (purple) TOMO only. The color version of this figure is available only in the electronic edition.

correlation between topographic amplification and smoothed curvature illustrates how local topographic features can cause seismic amplification. For example, our simulation predicts larger topographic amplification near the edges of steep slopes within the glacial units (e.g., nodes BM40, BM31, BM23, and BM14 labeled at x = 0, 350, 600, and 950 m, respectively, in the bottom panels of Fig. 11), which correspond to locations with larger positive curvature values (middle panel of Fig. 11a). This result is consistent with the observation of increased damage from the M_w 7.1 mainshock to residences throughout this neighborhood that are located close to steep slopes. On the other hand, our analysis shows that the correlation between the two variables tends to decline at higher frequencies (middle panel of Fig. 11b), suggesting that such a simplified model derived from a homogeneous medium (Maufroy *et al.*, 2015) needs corrections for higher frequencies when applied to realistic near-surface wavespeeds and highly complex topography.

Motivated by the unexpectedly large (~2*g*) ground motions at the NetQuake station NP.ARTY during the 2018 M_w 7.1 mainshock (Cramer and Jambo, 2019), we demonstrated how numerical simulation and local geological information can be combined as a powerful tool for analyzing complex seismic amplification. Building on insights from previous studies such as Mohammadi and Asimaki (2017), our simulations reveal that topographic effects and shallow geologic structure jointly contribute to site amplification and scattering, underscoring the importance of their coupled influence in the Chugiak area. These results highlight the significance of assessing local site response, even in regions outside major sedimentary basins.

DATA AND RESOURCES

The instrumentation for the nodal array deployed in Chugiak consists of 92 SmartSolo IGU-16HR 3C model nodes. These nodes have internal Global Positioning System (GPS) receivers, batteries, solid-state storage, and three-component (one vertical and two horizontal) 5 Hz geophones. The nodes maintain timing with microsecond accuracy and allow accurate determination of station locations using the built-in GPS receivers, even while buried by a few inches of soil. The nodes operated autonomously on battery power for ~30 days, recording continuously at 250 samples per second. The complete data set from this deployment is archived and available to the public at the EarthScope (formally Incorporated Research Institutions for Seismology [IRIS]) Data Management Center (DMC) in miniSEED data format using the U.S. Geological Survey (USGS) net code GM, and the station names range from BM01 to BM92. Metadata information for these stations is also available at the EarthScope DMC. We accessed the raw seismic data from the nodal array using the data fetch tool released by IRIS and removed the instrument response using poles and zeros through the Seismic Analysis Code (SAC, released by IRIS). The preprocessed strong-motion recordings used for model validation were retrieved from the Center for Engineering Strong Motion (CESMD), which require no further processing. We obtained moment tensor solutions and hypocenter locations of the three M_w 4.6–4.8 events via the USGS event pages (U.S. Geological Survey, Earthquake Hazards Program, 2017). The supplemental material also provides observation of seismic amplification for individual events along the nodal array, more detailed description about implementation of the basin structure, the point-source model, and the low-velocity taper (LVT).

DECLARATION OF COMPETING INTERESTS

The authors acknowledge that there are no conflicts of interest recorded.

ACKNOWLEDGMENTS

This research used resources of the Oak Ridge Leadership Computing Facility at the Oak Ridge National Laboratory, which is supported by the Office of Science of the U.S. Department of Energy under Contract Number DE-AC05-00OR22725. The research was supported by the U.S. Geological Survey (USGS), Department of the Interior, under USGS IPA OF 69 (REV. 2-89). The authors thank Mark Goldman, Coyn Criley, Joanne Chan, Jillian Holland, and Hailey Holland for their assistance in the nodal array deployment. The authors are grateful to Carl Tape and an anonymous reviewer for comments leading to an improved article.

Any use of trade, firm, or product names is for descriptive purposes only and does not imply endorsement by the U.S. Government.

REFERENCES

Aagaard, B. T., T. M. Brocher, D. Dolenc, D. Dreger, R. W. Graves, S. Harmsen, S. Hartzell, S. Larsen, and M. L. Zoback (2008). Ground-motion modeling of the 1906 San Francisco earthquake, part I: Validation using the 1989 Loma Prieta earthquake, *Bull. Seismol. Soc. Am.* **98,** no. 2, 989–1011, doi: 10.1785/0120060409.

Alaska Department of Natural Resources - Information Resource Management (2013). Alaska DNR DMLW Well Log Tracking System (WELTS), available at https://dnr.alaska.gov/welts (last accessed July 2023).

Alaska Earthquake Center, Univ. of Alaska Fairbanks (1987). Alaska Geophysical Network, doi: 10.7914/SN/AK.

Berg, E. M., F.-C. Lin, A. Allam, V. Schulte-Pelkum, K. M. Ward, and W. Shen (2020). Shear velocity model of Alaska via joint inversion of Rayleigh wave ellipticity, phase velocities, and receiver functions across the Alaska Transportable Array, *J. Geophys. Res.* **125,** no. 2, e2019JB018582, doi: 10.1029/2019JB018582.

Boore, D. M., and W. B. Joyner (1997). Site amplifications for generic rock sites, *Bull. Seismol. Soc. Am.* **87,** no. 2, 327–341, doi: 10.1785/BSSA0870020327.

Brocher, T. M. (2008). Compressional and shear-wave velocity versus depth relations for common rock types in Northern California, *Bull. Seismol. Soc. Am.* **98,** no. 2, 950–968, doi: 10.1785/0120060403.

Catchings, R. D., M. R. Goldman, J. H. Steidl, J. H. Chan, A. A. Allam, C. J. Criley, Z. Ma, D. S. Langermann, G. J. Huddleston, A. T. McEvilly, *et al.* (2020). Nodal seismograph recordings of the 2019 Ridgecrest earthquake sequence, *Seismol. Res. Lett.* **91,** no. 6, 3622–3633, doi: 10.1785/0220200203.

Cramer, C. H., and E. Jambo (2019). Impact of a larger fore-arc region on earthquake ground motions in South-Central Alaska including the 2018 M 7.1 Anchorage Inslab earthquake, *Seismol. Res. Lett.* **91,** no. 1, 174–182, doi: 10.1785/0220190183.

Cui, Y., E. Poyraz, K. B. Olsen, J. Zhou, K. Withers, S. Callaghan, J. Larkin, C. Guest, D. Choi, A. Chourasia, *et al.* (2013). Physics-based seismic hazard analysis on petascale heterogeneous supercomputers, *Proc. of the International Conf. on High Performance Computing, Networking, Storage and Analysis*, 1–12.

Dutta, U., N. Biswas, A. Martirosyan, S. Nath, M. Dravinski, A. Papageorgiou, and R. Combellick (2000). Delineation of spatial variation of shear wave velocity with high-frequency Rayleigh waves in Anchorage, Alaska, *Geophys. J. Int.* **143,** no. 2, 365–375, doi: 10.1046/j.1365-246X.2000.01240.x.

Eberhart-Phillips, D., D. H. Christensen, T. M. Brocher, R. Hansen, N. A. Ruppert, P. J. Haeussler, and G. A. Abers (2006). Imaging the transition from Aleutian subduction to Yakutat collision in central Alaska, with local earthquakes and active source data, *J. Geophys. Res.* **111,** no. B11, doi: 10.1029/2005JB004240.

Grapenthin, R., M. West, C. Tape, M. Gardine, and J. Freymueller (2018). Single-frequency instantaneous GNSS velocities resolve dynamic ground motion of the 2016 Mw 7.1 Iniskin, Alaska, earthquake, *Seismol. Res. Lett.* **89,** no. 3, 1040–1048, doi: 10.1785/0220170235.

Hu, Z., K. B. Olsen, and S. M. Day (2022a). 0–5 Hz deterministic 3-D ground motion simulations for the 2014 La Habra, California, earthquake, *Geophys. J. Int.* **230,** no. 3, 2162–2182, doi: 10.1093/gji/ggac174.

Hu, Z., K. B. Olsen, and S. M. Day (2022b). Calibration of the near-surface seismic structure in the SCEC community velocity model version 4, *Geophys. J. Int.* **230,** no. 3, 2183–2198, doi: 10.1093/gji/ggac175.

Jibson, R. W., A. R. R. Grant, R. C. Witter, K. E. Allstadt, E. M. Thompson, and A. M. Bender (2019). Ground failure from the anchorage, Alaska, earthquake of 30 November 2018, *Seismol. Res. Lett.* **91,** no. 1, 19–32, doi: 10.1785/0220190187.

Kopczynski, S. E., S. E. Kelley, T. V. Lowell, E. B. Evenson, and P. J. Applegate (2017). Latest Pleistocene advance and collapse of the Matanuska – Knik glacier system, Anchorage Lowland, southern Alaska, *Quaternary Sci. Rev.* **156,** 121–134, doi: 10.1016/j.quascirev.2016.11.026.

Kroner, C., T. Jahr, S. Kuhlmann, and K. D. Fischer (2005). Pressure-induced noise on horizontal seismometer and strainmeter records evaluated by finite element modelling, *Geophys. J. Int.* **161,** no. 1, 167–178, doi: 10.1111/j.1365-246X.2005.02576.x.

Martin-Short, R., R. Allen, I. D. Bastow, R. W. Porritt, and M. S. Miller (2018). Seismic Imaging of the Alaska subduction zone: Implications for slab geometry and volcanism, *Geochem. Geophys. Geosys.* **19,** no. 11, 4541–4560, doi: 10.1029/2018GC007962.

Maufroy, E., V. M. Cruz-Atienza, F. Cotton, and S. Gaffet (2015). Frequency-scaled curvature as a proxy for topographic site-effect amplification and ground-motion variability, *Bull. Seismol. Soc. Am.* **105,** no. 1, 354–367, doi: 10.1785/0120140089.

Mohammadi, K., and D. Asimaki (2017). Topography effects are not dominated by ground surface geometry: A site effects paradox, in *Geotechnical Frontiers 2017: Seismic Performance and Liquefaction*, T. L. Brandon and R. J. Valentine (Editors), American Society of Civil Engineers, 171–181, doi: 10.1061/9780784480489.018.

Moschetti, M. P., E. M. Thompson, J. Rekoske, M. G. Hearne, P. M. Powers, D. E. McNamara, and C. Tape (2019). Ground-motion amplification in cook inlet region, Alaska, from intermediate-depth earthquakes, including the 2018 Mw 7.1 Anchorage earthquake, *Seismol. Res. Lett.* **91,** no. 1, 142–152, doi: 10.1785/0220190179.

Nayak, A., D. Eberhart-Phillips, N. A. Ruppert, H. Fang, M. M. Moore, C. Tape, D. H. Christensen, G. A. Abers, and C. H. Thurber (2020). 3D seismic velocity models for Alaska from joint tomographic inversion of body-wave and surface-wave data, *Seismol. Res. Lett.* **91,** no. 6, 3106–3119, doi: 10.1785/0220200214.

Nie, S., Y. Wang, K. B. Olsen, and S. M. Day (2017). Fourth-order staggered-grid finite-difference seismic wavefield estimation using a discontinuous mesh interface (WEDMI) fourth-order staggered-grid finite-difference Seismic WEDMI, *Bull. Seismol. Soc. Am.* **107,** no. 5, 2183–2193, doi: 10.1785/0120170077.

Olsen, K. B. (1994). Simulation of three-dimensional wave propagation in the Salt Lake Basin, *Ph.D. Thesis*, University of Utah, Salt Lake City, Utah, 157 pp.

Olsen, K. B., S. M. Day, and C. R. Bradley (2003). Estimation of Q for long-period (>2 sec) waves in the Los Angeles Basin, *Bull. Seismol. Soc. Am.* **93,** no. 2, 627–638, doi: 10.1785/0120020135.

O'Reilly, O., T. Yeh, K. B. Olsen, Z. Hu, A. Breuer, D. Roten, and C. A. Goulet (2021). A high-order finite-difference method on staggered curvilinear grids for seismic wave propagation applications with topography, *Bull. Seismol. Soc. Am.* **112,** no. 1, 3–22, doi: 10.1785/0120210096.

Ruppert, N. A., and R. C. Witter (2019). Preface to the focus section on the 30 November 2018 Mw 7.1 Anchorage, Alaska, earthquake, *Seismol. Res. Lett.* **91,** no. 1, 16–18, doi: 10.1785/0220190344.

Schmoll, H. R., L. A. Yehle, and R. G. Updike (1999). Summary of quaternary geology of the municipality of Anchorage, Alaska, *Quaternary Int.* **60,** no. 1, 3–36, doi: 10.1016/S1040-6182(99)00004-X.

Shellenbaum, D. P., L. S. Gregersen, and P. R. Delaney (2010). Top Mesozoic unconformity depth map of the Cook Inlet Basin, Alaska, *Technical Rept. RI 2010-2*, Alaska Division of Geological and Geophysical Surveys.

Silwal, V., C. Tape, and A. Lomax (2018). Crustal earthquakes in the Cook Inlet and Susitna region of southern Alaska, *Tectonophysics* **745,** 245–263, doi: 10.1016/j.tecto.2018.08.013.

Smith, K., and C. Tape (2019). Seismic response of Cook Inlet Sedimentary Basin, Southern Alaska, *Seismol. Res. Lett.* **91,** no. 1, 33–55, doi: 10.1785/0220190205.

Thornley, J., J. Douglas, U. Dutta, and Z. J. Yang (2022). Engineering site response analysis of Anchorage, Alaska, using site amplifications and random vibration theory, *Earthq. Spectra* **38,** no. 2, 1103–1123, doi: 10.1177/87552930211065482.

U.S. Geological Survey (1931). United States National Strong-Motion Network, doi: 10.7914/SN/NP.

U.S. Geological Survey (2020). 3D elevation program 1-meter resolution digital elevation model (Published 20200330).

U.S. Geological Survey, Earthquake Hazards Program (2017). Advanced National Seismic System (ANSS) comprehensive catalog of earthquake events and products, doi: 10.5066/F7MS3QZH.

Wang, Y., and C. Tape (2014). Seismic velocity structure and anisotropy of the Alaska subduction zone based on surface wave tomography, *J. Geophys. Res.* **119,** no. 12, 8845–8865, doi: 10.1002/2014JB011438.

Ward, K. M. (2015). Ambient noise tomography across the southern Alaskan Cordillera, *Geophys. Res. Lett.* **42,** no. 9, 3218–3227, doi: 10.1002/2015GL063613.

Ward, K. M., and F.-C. Lin (2018). Lithospheric structure across the alaskan cordillera from the joint inversion of surface waves and receiver functions, *J. Geophys. Res.* **123,** no. 10, 8780–8797, doi: 10.1029/2018JB015967.

West, M. E., A. Bender, M. Gardine, L. Gardine, K. Gately, P. Haeussler, W. Hassan, F. Meyer, C. Richards, N. Ruppert, *et al.* (2019). The 30 November 2018 Mw 7.1 Anchorage earthquake, *Seismol. Res. Lett.* **91,** no. 1, 66–84, doi: 10.1785/0220190176.

Withers, K. B., K. B. Olsen, and S. M. Day (2015). Memory-efficient simulation of frequency-dependent Q, *Bull. Seismol. Soc. Am.* **105,** no. 6, 3129–3142, doi: 10.1785/0120150020.

Yeh, T., and K. B. Olsen (2023). Fault damage zone effects on ground motions during the 2019 Mw 7.1 Ridgecrest, California, earthquake, *Bull. Seismol. Soc. Am.* doi: 10.1785/0120220249.

Yeh, T.-Y., and K. B. Olsen (2024). Simulation of 0–7.5 Hz physics-based nonlinear ground motions for maximum credible earthquake scenarios at the Long Valley Dam, CA, *Earthq. Spectra* doi: 10.1177/87552930231226135.

Manuscript received 30 December 2024
Published online 22 August 2025